Scripta Materialia 162 (2019) 451–455

Contents lists available at ScienceDirect

Scripta Materialia

journal homepage: www.elsevier.com/locate/scriptamat

Variable temperature micropillar compression to reveal <a> basal slip properties of Zircaloy-4

Siyang Wang *, Finn Giuliani, T. Ben Britton

Department of Materials, Royal School of Mines, Imperial College London, London, SW7 2AZ, UK

ARTICLE INFO

Article history:
Received 28 September 2018
Received in revised form 7 December 2018
Accepted 10 December 2018
Available online 19 December 2018

Keywords:
Zirconium
Critical resolved shear stress
Micropillar compression
Elevated temperature

ABSTRACT

Zircaloy-4 is widely used as nuclear fuel cladding materials, where it is important to understand the mechanical properties between room temperature and reactor operating temperatures (around 623 K). To aid in this understanding, we have performed compression tests on micropillars aligned to activate <a> basal slip across this temperature range. Engineering analysis of the results indicates that the plastic yield follows a thermally activated constitutive law. We also observe the nature of the slip bands formed on the side surface of our pillars and see characteristic 'bulging' that tends to localise as temperature increases.

Zirconium alloys are used as fuel cladding materials in water-based nuclear reactors and are often employed at around 623 K [1], and therefore the structural integrity of the reactor core depends strongly on the service temperature mechanical performance of the cladding material. Like most of other hexagonal close packed (HCP) materials, the known deformation modes of Zr include plastic slip on the basal, prismatic and pyramidal planes as well as twinning [2]. For Zr, <a> prismatic slip has the lowest critical resolved shear stress (CRSS, τ_{CRSS}) at room temperature and is therefore the easiest deformation mode [3]. Akhtar [4] measured the CRSS of <a> basal slip in Zr between 873 and 1123 K, however below this temperature range the deformation of single crystal samples favourably orientated for <a> basal slip was accommodated instead by prismatic slip and twinning and so variations within this range were not measured. However, in Zr the activation of <a> basal slip at room temperature has been observed locally where the stress is concentrated and deformation rate is high [5], as well as around Zr hydride packets in transmission electron microscope (TEM) foils [6,7]. Gong et al. [3] used microcantilever bending tests to show that the ratio of CRSS values for <a> prism to <a> basal to <c + a> pyramidal slip is 1:1.3:3.5 and these results were suitable for crystal plasticity modelling of plastic flow in a macroscopic textured polycrystal. Recent work by Caillard et al. [7] observed the glide of <a> dislocations on the basal plane in Zr from room temperature up to 573 K under suitable stress states through *in situ* TEM experiments. The influence of stress state on the basal-prismatic cross slip behaviour indicates that basal slip is only slightly harder than prismatic slip and is a primary slip system for Zr at and above room temperature. Furthermore, the increasingly rapid motion of screw dislocations on the basal plane with increasing temperature is indicative of the fact that <a> basal slip is strongly thermally activated and becomes nearly athermal at 573 K.

Attempts have been made experimentally to study the high temperature deformation behaviour of bulk Zr alloys [8–16], and the results are briefly attributed to two types of mechanisms, including the thermally-activated dislocation glide and the climb-driven dislocation annihilation and recovery [17]. Computational modelling was used to evaluate the effect of temperature on the relative contributions of different deformation modes to the macroscopic response of polycrystalline Zr [18,19]. However, the lack of high temperature experimental data on the strength of the slip and twinning deformation modes has restricted the accuracy of the models in predicting the experimental material response. Therefore, knowledge of the properties of single deformation modes at high temperatures, especially near the service temperature of Zircaloy claddings, would be advantageous for developing the current understanding of the deformation of Zr at high temperatures and improving the in-service mechanical performance of the material.

Micromechanical testing (such as micropillar compression and microcantilever bending) on single crystal specimens fabricated within individual grains with specific crystal orientations provides the opportunity of activating and studying a single targeted slip system per test [2]. Successful implementation of micropillar compression tests on studying mechanical behaviour of Mg [20–23] and Ti [24–29] alloys shows the potential of applying this technique to other HCP materials such as Zr. In the past decade, development of the state-of-art experimental apparatus has allowed micropillar compression tests to be carried out at elevated temperatures. This provides a way of investigating the high temperature mechanical properties of a wide range of materials including Ni superalloy [30], nanocrystalline Ni [31], Cu [32], Ta

* Corresponding author.
E-mail address: siyang.wang15@imperial.ac.uk (S. Wang).

https://doi.org/10.1016/j.scriptamat.2018.12.014
1359-6462/

and W [33], Cu/TiN multilayers [34], Au-based metallic glass [35], LiF [36], CrN-based hard coating [37] and $MgAl_2O_4$ spinel [38]. The capability of testing single crystal specimens under a (near) uniaxial stress state at elevated temperatures has made this technique a promising method to directly extract fundamental in-service properties of industrial materials employed at high temperatures. The motivation of this work is to utilise the advantages of elevated temperature micropillar compression tests and to explore the properties of <a> basal slip system in Zircaloy-4 and their temperature dependence between room temperature and 623 K, the typical service temperature of Zircaloy fuel claddings.

Commercial Zircaloy-4 with a nominal chemical composition of Zr-1.5%Sn-0.2%Fe-0.1%Cr in weight [39] was supplied in the form of rolled and recrystallised plate with equiaxed grains. The average grain size is about 11 μm. The texture of the plate is typical of its processing history, with basal poles tilted ±30° from the normal direction (ND) to the transverse direction (TD). An approximately 10 mm × 10 mm × 1.5 mm cuboid was cut from the plate and then heat treated for 336 h at 800 °C in Ar atmosphere to produce 'blocky alpha' grains with an average size >200 μm [40]. The sample was then ground, mechanically polished, and finally electropolished in a solution of 10 vol% perchloric acid in methanol at −45 °C for 90 s, under 30 V applied voltage to remove the surface stress layer.

We selected crystals that would activate <a> basal slip. Electron backscatter diffraction (EBSD) scanning was carried out on an FEI Quanta scanning electron microscope (SEM) equipped with a Bruker eFlash^{HD} EBSD camera using 20 kV beam voltage. An approximately 0.3 mm^2 grain with Euler angles $[\varphi_1,\Phi,\varphi_2] = [36°,44°,349°]$ was found which has Schmid factors of 0.49, 0.33 and 0.16 for the three available <a> basal slip systems while the loading axis is perpendicular to the sample surface. The Schmid factor for the easiest <a> prismatic slip system is 0.24, less than half of that for the easiest <a> basal slip system. The easiest pyramidal slip system has a Schmid factor of 0.39, however the high strength of this slip mode has made its activation unlikely to occur. Square micropillars with 5 μm mid-height width and 15 μm height were hence fabricated within this grain using Ga focused ion beam (FIB) milling on an FEI Helios Nanolab 600 Dualbeam microscope (Fig. 1 (a)). Thermo Scientific NanoBuilder software was used to set up the FIB patterning profile. The acceleration voltage of the FIB was set to 30 kV and a series of FIB beam current from 21 nA down to 1 nA was used. High current beam was applied to produce a 50 μm-diameter trench around the micropillar in order to achieve *in situ* visualisation of the micropillar during the subsequent tests, while low current beam was used for the final tailoring of the micropillar contour. *In situ* SEM micropillar compression tests were carried out using a displacement-controlled Alemnis nanoindenter coupled with a high temperature module (as shown in Fig. 1(b)), on the FEI Quanta SEM. A 10 μm-diameter circular flat punch indenter was used in order to achieve a uniaxial stress state for the compression tests (Fig. 1 (c)). The loading and unloading speed used were 5 nm/s and 50 nm/s, respectively, resulting in a compressive strain rate of 3.3×10^{-4} s^{-1} during the tests. Thermal equilibrium between the sample and the indenter tip at each testing temperature was achieved using a free surface indentation method under pseudo load-controlled mode as described in detail in [41] to minimize the thermal drift.

In situ SEM micropillar compression tests were conducted at five different temperatures: 298 K, 373 K, 473 K, 573 K and 623 K. The tests were done successively from low temperature to high temperature. Two micropillars were tested at each temperature and all micropillars were deformed to a displacement of 1.5 μm. The engineering stress-strain curves obtained for all tests are plotted in Fig. 2 (a). The engineering stress (σ_{eng}) and engineering strain (ε_{eng}) was calculated by dividing the load value with the mid-height cross sectional area of the micropillar and dividing the displacement value with the height of the

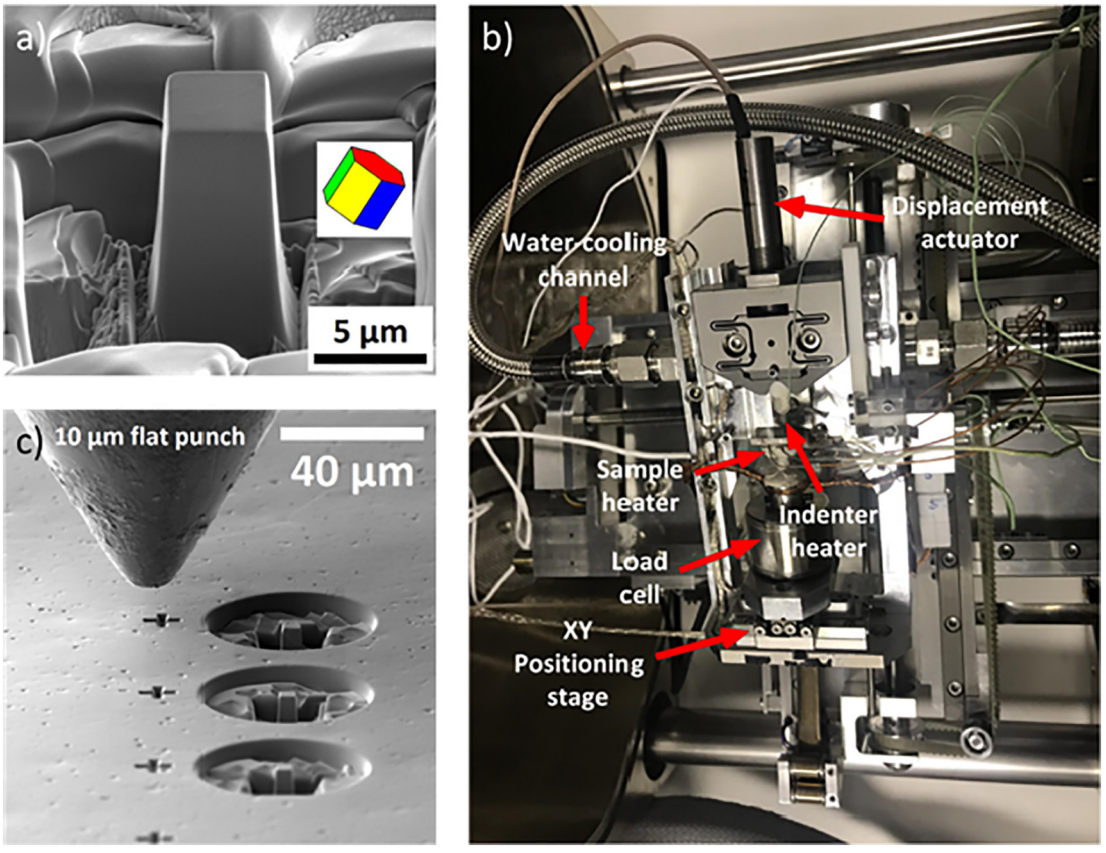

Fig. 1. (a) Secondary electron (SE) image of a micropillar fabricated with FIB, with an insert of the unit cell respenstation of the crystal orientation, (b) high temperature Alemnis nanoindentation system for *in situ* compression tests and (c) SE image showing the flat punch indenter and an array of micropillars.

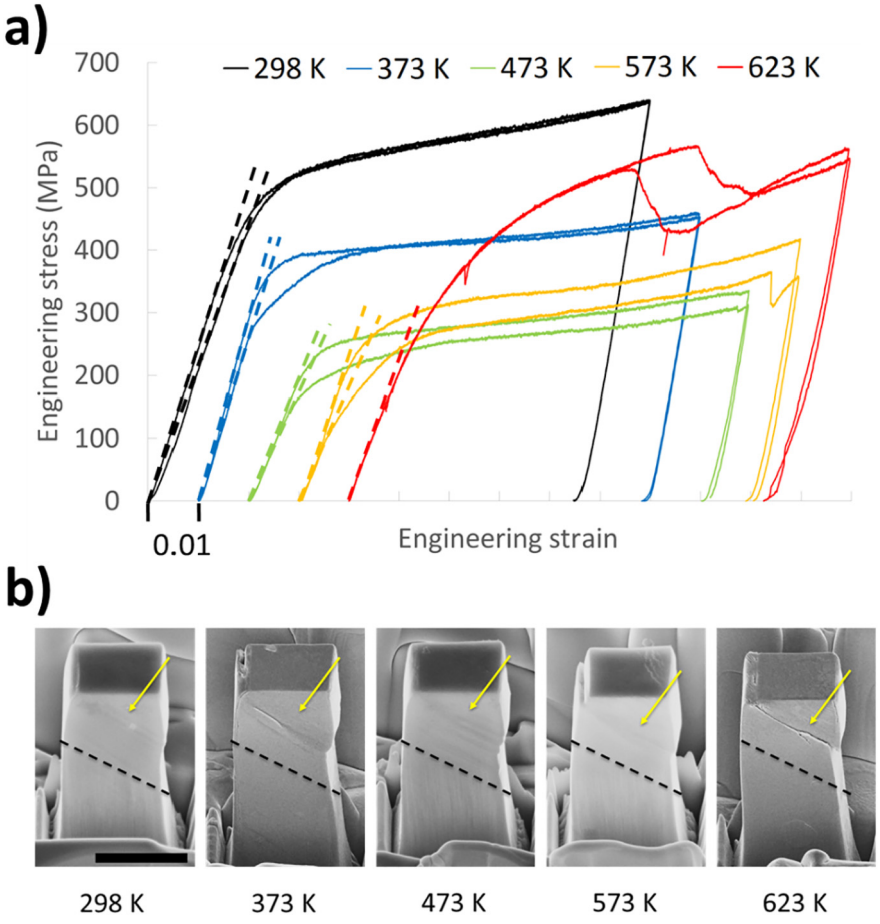

Fig. 2. (a) Engineering stress-strain curves for micropillar compression tests at various temperatures and (b) post-deformation SE images of the micropillars at each testing temperature, with arrows highlighting the slip bands. The length of the scale bar is 5 μm.

micropillar, respectively (as per Jun et al. [26,27]). There is good consistency between both micropillars tested for each temperature and significant variations with temperature.

Fig. 2 (b) shows the SEM micrographs of the micropillars captured when the compression tests were complete. Dashed lines overlaid on the images show the theoretical orientation of the <a> basal slip trace derived from the orientation of the crystal measured by EBSD. Slip bands could be observed on all micropillars at a similar position on the pillar body, between the top left corner and the right edge of the micropillars. The parallel between the observed slip bands and the dashed lines confirms the activation of <a> basal slip at all testing temperatures, and there was no evidence of the activation of other deformation modes within the SEM micrographs. Deformation of pillars at room temperature, 373 K and 473 K tends to result in the formation of multiple closely spaced slip bands on the basal plane, ultimately leading to several small slip steps at the right edge of the micropillars. As the temperature reaches 573 K, the deformation becomes more heterogeneous. Further increasing the temperature to 623 K, the plastic strain is highly localised and only one distinct slip band and a sharp slip step can be observed. The slip step was formed while the slip band reached the edge of the micropillar during the deformation process, causing the abrupt stress drops at around 6% to 7% engineering strain on the engineering stress-strain response (Fig. 2 (a)).

The CRSS for <a> basal slip is then extracted from the engineering stress-strain curve measured for each test, by multiplying the yield stress by the Schmid factor for <a> basal slip. Determination of the yield stress was done by plotting the derivative of σ_{eng} with respect to ε_{eng} against ε_{eng}, and the first deviation from the elastic plateau was regarded as the yield point. The CRSS values were then plotted against temperature in Fig. 3, along with literature results for commercially pure (CP) Zr [3] and Zr single crystal with unspecified composition [4]. Zircaloy-4 is a dilute Zr alloy and has very similar mechanical properties to CP Zr (ASTM standards B352/B352M and B551/B551M), therefore our results from Zircaloy-4 are likely reasonable. The two CRSS values obtained through micropillar compression tests at room temperature, 178 MPa and 155 MPa, are both well within the 95% confidence interval of 204 ± 66 MPa which is the size independent CRSS for <a> basal slip in CP Zr at room temperature. This implies that the size effect is minimised here by testing relatively large micropillars and therefore the results at all temperatures should be representative of the macroscopically relevant mechanical properties.

A strong temperature dependence of the CRSS for <a> basal slip could be seen in Fig. 3 as the CRSS decrease significantly with increasing temperature between 298 and 623 K, revealing the strong thermally activated character of this slip system. An exponential curve ($\tau_{CRSS} = 11.3\, e^{\frac{807.7}{T}}$) is found through least squares fitting to describe the CRSS-temperature relationship. The gradient of the curve is steep below 473 K, and becomes gentle above 573 K, where the temperature dependence of the <a> basal slip strength becomes weak.

A noticeable difference in the strain hardening behaviour of the micropillars deformed at different temperatures can be observed on the engineering stress-strain curves (Fig. 2 (a)). For the tests conducted at between 298 K and 573 K, two strain hardening stages can be observed on each of the engineering stress-strain curves. The strain hardening rates are nearly constant after the yield point until around 6% engineering strain, and from 6% to 10% engineering strain an increasing trend of the strain hardening rates can be seen. It has been found that the engineering stress levels at the points where the changes in the

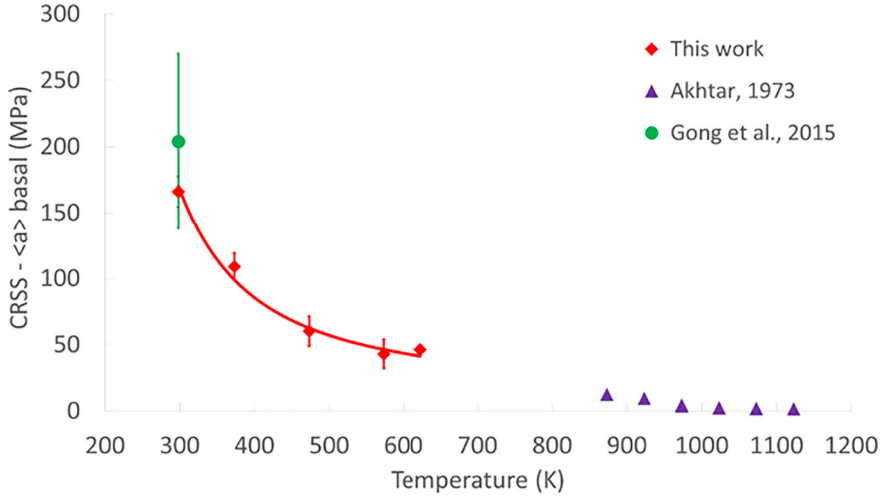

Fig. 3. The variation of CRSS for <a> basal slip with temperature [3,4].

strain hardening rate occur are all approximately 1.5 times the yield stresses, similar to the ratio between the Schmid factors of the easiest (0.49) and the second easiest (0.33) <a> basal slip systems. It is therefore speculated that the observed increase in the strain hardening rates after 6% engineering strain is due to the activation of the second <a> basal slip system and the consequent interactions between the dislocations with different <a> Burgers vectors gliding on the basal plane. The strain hardening rate (the derivative of σ_{eng} with respect to ε_{eng}) at 5% engineering strain for each test was extracted and its variation with temperature is shown in Fig. 4. The strain hardening rates are extracted from the engineering stress-strain response rather than true stress-strain response and we note that care must be taken in interpretation due to the taper of the micropillars and the strain localisation observed.

Broadly, the hardening rate for tests between room temperature and 573 K are approximately half that of the test at 623 K. A similar temperature dependence has been noticed for the extent of strain localisation, as shown in Fig. 2 (b). It is therefore inferred that the formation of localised slip band is associated with high hardening rate. This has also been observed for <a> basal slip in α-Ti at room temperature by Jun et al. [27], and was attributed to strong resistance to dislocation motion from pinning obstacles and complicated dislocation-dislocation interactions. We see slip is more localised at 623 K and the nature of the slip band/shear together with the stress-strain response implies that the dislocations are behaving differently, which could be a result of a change in the operation of <a> basal dislocations or the interaction with dislocations gliding on other systems. The temperature dependency of <a> prismatic slip in pure Zr has been found to vary significantly with oxygen content [42] and is yet to be established in Zircaloy-4. Future investigation into the change in the CRSS for <a> prismatic slip with temperature in Zircaloy-4 may help better understand the hardening behaviour observed here.

In summary, compression tests were carried out on single crystal Zircaloy-4 micropillars between room temperature and 623 K with an effective strain rate of $3.3 \times 10^{-4}\ s^{-1}$. Post-deformation SEM micrographs confirmed the activation of <a> basal slip system at all testing temperatures. The CRSS for <a> basal slip at the testing temperatures were unambiguously determined and an obvious temperature dependence was found. The variation of CRSS within the testing temperature range is described well by $\tau_{CRSS} = 11.3\, e^{\frac{807.7}{T}}$, indicating the strong thermally activated nature of the <a> basal slip system. Through comparison with the size independent CRSS of CP Zr, it has been validated that the CRSS values extracted in the present work is representative of the macroscopically relevant mechanical properties. The change in slip band structure with temperature implies a change in the <a> basal slip mechanism with temperature. Slip localisation is promoted at elevated

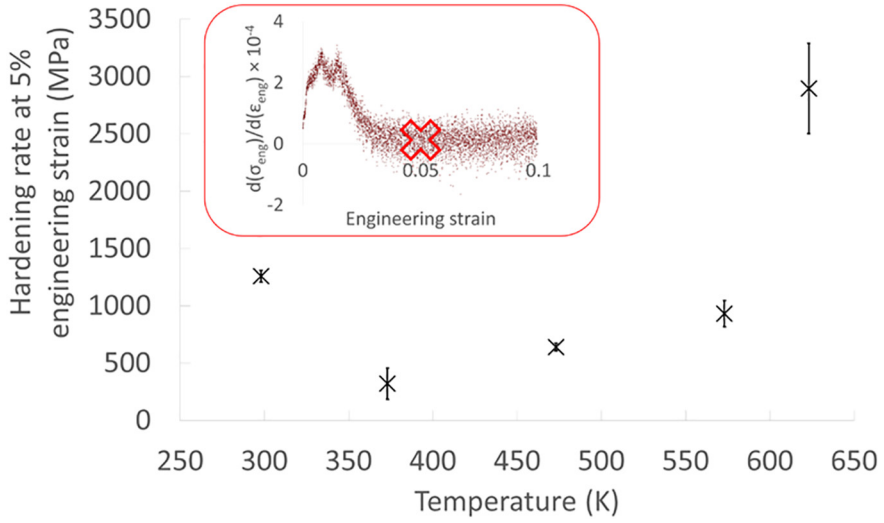

Fig. 4. The variation of hardening rate at 5% engineering strain with temperature, with an insert showing the extraction of the hardening rate from a stress-strain response.

temperatures, as observed in the formation of the slip step on the side of our pillars, a change in hardening, and a reduction in the critical resolved shear stress with temperature. Together these imply that the <a> basal slip mechanism changes with temperature which should be related to the viscoplastic nature of <a> basal slip in Zircaloy-4. This could be caused by a change in (time dependant) dislocation mechanism [7], potentially due to dislocation glide, local climb, or cross slip.

Acknowledgement

The authors thank Vivian Tong and Tommaso Giovannini for useful discussions, and Suki Adande for developing the NanoBuilder FIB patterning script used for the micropillar fabrication in this work. TBB and SW acknowledge support from HexMat (EPSRC EP/K034332/1). TBB thanks the Royal Academy of Engineering for funding his Research Fellowship. The *in situ* testing was performed on the FEI Quanta SEM which was supported by the Shell AIMS UTC and is housed in the Harvey Flower EM suite at Imperial College London. The data in this paper can be found on Zenodo - https://zenodo.org/badge/DOI/10.5281/zenodo.2222400.

References

[1] J.C.A. Gaspar Jr., M.L. Moreira, P.A.B. Desampaio, Proc. Int. Conf. Nucl. Energy New Eur. (2011) 814.
[2] T.B. Britton, F.P.E. Dunne, A.J. Wilkinson, Proc. R. Soc. A Math. Phys. Eng. Sci. 471 (2015) 20140881, https://doi.org/10.1098/rspa.2014.0881.
[3] J. Gong, T. Benjamin Britton, M.A. Cuddihy, F.P.E. Dunne, A.J. Wilkinson, Acta Mater. 96 (2015) 249–257.
[4] A. Akhtar, Acta Metall. 21 (1973) 1–11.
[5] J.I. Dickson, G.B. Craig, J. Nucl. Mater. 40 (1971) 346–348.
[6] J.E. Bailey, Acta Metall. 11 (1963) 267–280.
[7] D. Caillard, M. Gaumé, F. Onimus, Acta Mater. 155 (2018) 23–34.
[8] J.L. Derep, S. Ibrahim, R. Rouby, G. Fantozzi, Acta Metall. 28 (1980) 607–619.
[9] C. Grosjean, D. Poquillon, J.C. Salabura, J.M. Cloué, Mater. Sci. Eng. A 510–511 (2009) 332–336.
[10] J.H. Moon, P.E. Cantonwine, K.R. Anderson, S. Karthikeyan, M.J. Mills, J. Nucl. Mater. 353 (2006) 177–189.
[11] C. Nam, B.K. Choi, M.H. Lee, Y.H. Jeong, J. Nucl. Mater. 305 (2002) 70–76.
[12] H. Siethoff, K. Ahlborn, Scr. Metall. 21 (1987) 1439–1444.
[13] M. Rautenberg, X. Feaugas, D. Poquillon, J.M. Cloué, Acta Mater. 60 (2012) 4319–4327.
[14] W.R. Thorpe, I.O. Smith, J. Nucl. Mater. 75 (1978) 209–219.
[15] I. Charit, K.L. Murty, J. Nucl. Mater. 374 (2008) 354–363.
[16] T.A. Hayes, M.E. Kassner, Metall. Mater. Trans. A 37 (2006) 2389–2396.
[17] D. Caillard, M. Rautenberg, X. Feaugas, Acta Mater. 87 (2015) 283–292.
[18] M. Knezevic, M. Zecevic, I.J. Beyerlein, J.F. Bingert, R.J. McCabe, Acta Mater. 88 (2015) 55–73.
[19] G. Bharat Reddy, A. Sarkar, R. Kapoor, A.K. Kanjarla, Mater. Sci. Eng. A 734 (2018) 210–223.
[20] C.M. Byer, K.T. Ramesh, Acta Mater. 61 (2013) 3808–3818.
[21] E. Lilleodden, Scr. Mater. 62 (2010) 532–535.
[22] K.E. Prasad, K. Rajesh, U. Ramamurty, Acta Mater. 65 (2014) 316–325.
[23] J. Ye, R.K. Mishra, A.K. Sachdev, A.M. Minor, Scr. Mater. 64 (2011) 292–295.
[24] Q. Sun, Q. Guo, X. Yao, L. Xiao, J.R. Greer, J. Sun, Scr. Mater. 65 (2011) 473–476.
[25] Q. Yu, Z.-W. Shan, J. Li, X. Huang, L. Xiao, J. Sun, E. Ma, Nature 463 (2010) 335–338.
[26] T.S. Jun, G. Sernicola, F.P.E. Dunne, T.B. Britton, Mater. Sci. Eng. A 649 (2016) 39–47.
[27] T.-S. Jun, Z. Zhang, G. Sernicola, F.P.E. Dunne, T.B. Britton, Acta Mater. 107 (2016) 298–309.
[28] Z. Zhang, T.S. Jun, T.B. Britton, F.P.E. Dunne, J. Mech. Phys. Solids 95 (2016) 393–410.
[29] Z. Zhang, T.S. Jun, T.B. Britton, F.P.E. Dunne, Acta Mater. 118 (2016) 317–330.
[30] S. Korte, R.J. Stearn, J.M. Wheeler, W.J. Clegg, J. Mater. Res. 27 (2012) 167–176.
[31] G. Mohanty, J.M. Wheeler, R. Raghavan, J. Wehrs, M. Hasegawa, S. Mischler, L. Philippe, J. Michler, Philos. Mag. 95 (2015) 1878–1895.
[32] J.M. Wheeler, C. Kirchlechner, J.S. Micha, J. Michler, D. Kiener, Philos. Mag. 96 (2016) 3379–3395.
[33] O. Torrents Abad, J.M. Wheeler, J. Michler, A.S. Schneider, E. Arzt, Acta Mater. 103 (2016) 483–494.
[34] R. Raghavan, J.M. Wheeler, D. Esqué-de los Ojos, K. Thomas, E. Almandoz, G.G. Fuentes, J. Michler, Mater. Sci. Eng. A 620 (2014) 375–382.
[35] S.X. Song, Y.H. Lai, J.C. Huang, T.G. Nieh, Appl. Phys. Lett. 94 (2009) 92–95.
[36] R. Soler, J.M. Wheeler, H.J. Chang, J. Segurado, J. Michler, J. Llorca, J.M. Molina-Aldareguia, Acta Mater. 81 (2014) 50–57.
[37] J.M. Wheeler, R. Raghavan, V. Chawla, M. Morstein, J. Michler, Surf. Coat. Technol. 254 (2014) 382–387.
[38] S. Korte, W.J. Clegg, Scr. Mater. 60 (2009) 807–810.
[39] D.O. Northwood, Mater. Des. 6 (1985) 58–70.
[40] V. Tong, B. Britton, Acta Mater. 129 (2017) 510–520.
[41] J.M. Wheeler, J. Michler, Rev. Sci. Instrum. 84 (2013).
[42] A. Akhtar, A. Teghtsoonian, Acta Metall. 19 (1971) 655–663.